The Influence of Large-Scale Radiation Anomalies on Tropical Cyclone Frequency

TSUNG-LIN HSIEH,[a] BOSONG ZHANG,[b] WENCHANG YANG,[c] GABRIEL A. VECCHI,[a,b,c] MING ZHAO,[d] BRIAN J. SODEN,[e] AND CHENGGONG WANG[b]

[a] *High Meadows Environmental Institute, Princeton University, Princeton, New Jersey*
[b] *Program in Atmospheric and Oceanic Sciences, Princeton University, Princeton, New Jersey*
[c] *Department of Geosciences, Princeton University, Princeton, New Jersey*
[d] *NOAA/Geophysical Fluid Dynamics Laboratory, Princeton, New Jersey*
[e] *Rosenstiel School of Marine and Atmospheric Science, University of Miami, Miami, Florida*

(Manuscript received 18 July 2022, in final form 12 April 2023, accepted 17 April 2023)

ABSTRACT: The response of tropical cyclone (TC) frequency to sea surface warming is uncertain in climate models. We hypothesize that one source of uncertainty is the anomalies of large-scale atmospheric radiation in response to climate change, and whose influence on TC frequency is investigated. Given two atmospheric models with opposite TC frequency responses to uniform sea surface warming, we interchange their atmospheric radiation anomalies in experiments with prescribed radiative heating rates. The largest model discrepancy occurs in the western North Pacific, where the TC frequency tends to increase with anomalous large-scale ascent caused by prescribed positive radiation anomalies, while the TC frequency tends to decrease with anomalous large-scale descent caused by prescribed negative radiation anomalies. The model spread in TC frequency response is approximated by the model spread in the frequency response of pre-TC vortices (seeds), which is explained by changes in the large-scale circulation using a downscaling formula known as the seed propensity index. We further generalize the index to predict the influence of large-scale radiation anomalies on TC seed frequency. The results show that model spread in TC and seed frequency response can be reduced when constraining the large-scale radiation anomalies.

SIGNIFICANCE STATEMENT: It is difficult to predict whether tropical cyclones will occur more or less frequently in the future and by how much. We show that tropical cyclone frequency is strongly influenced by the global pattern of heating and cooling due to radiation, a process that has been neglected in existing theories. Our theory improves understanding of how tropical cyclones respond to climate change, explaining why one model may predict a frequency increase while a different but equally realistic model may predict a frequency decrease. One reason for the difficulty in predicting tropical cyclone frequency is found to be the difficulty in predicting how global cloud distribution will change in the future.

KEYWORDS: Tropical cyclones; Climate change; Radiation

1. Introduction

The frequency and geographic distribution of tropical cyclones (TCs) change with the climate. While state-of-the-art global climate models provide more reliable projections on aspects like the global-mean precipitation rate, projections of TC frequency are less certain. TC frequency depends on a number of local environmental variables, such as the potential intensity, saturation deficit, and background vorticity (Emanuel 2010). These variables have distinct responses to warming and have different geographic patterns, and their combined effect is highly uncertain.

The response of radiative fluxes to climate change, particularly those associated with clouds, is a major source of uncertainty in the sensitivity of global-mean surface temperature to greenhouse gas concentration (Zelinka et al. 2020). Top-of-atmosphere radiative fluxes are important terms in Earth's energy budget. They are not uniform in space, and their global-mean magnitudes are related to the pattern of sea surface temperature (SST) response (Stevens et al. 2016), which is also uncertain across climate models.

While the uncertainty in TC frequency projection may be caused in part by different SST response patterns in coupled global climate models (Knutson et al. 2020), atmospheric model experiments with identical SST perturbations have shown a similar range of uncertainty in TC frequency response (Yamada et al. 2021; Hsieh et al. 2022). In particular, Hsieh et al. (2022) showed that two atmospheric models with different parameterizations of convection and most other settings identical, namely, the High Resolution Atmospheric Model (HiRAM) and Atmospheric Model, version 2.5 (AM2.5), developed at the Geophysical Fluid Dynamics Laboratory, generate opposite TC frequency responses to uniform SST increase. The largest model inconsistency occurs in the western North Pacific. In this region, the

Denotes content that is immediately available upon publication as open access.

Corresponding author: Tsung-Lin Hsieh, hsiehtl@princeton.edu

Publisher's Note: This article was revised on 1 August 2023 to include an additional acknowledgment that was missing from the Acknowledgments section when originally published.

DOI: 10.1175/JCLI-D-22-0449.1

models show opposite radiative heating rate anomalies, but the relationship between TC frequency response and radiative heating rate anomalies remains unclear.

We pose the hypothesis that *large-scale radiative heating rate anomalies affect TC frequency through the influence on large-scale vertical velocity and pre-TC vortices, known as TC seeds*. The chain of logic is the following, and it will be expressed quantitatively in section 2. In response to global warming, model spread in seed frequency has a leading-order impact on model spread in TC frequency (Yamada et al. 2021; Hsieh et al. 2022). Other changes in environmental variables, such as the vertical wind shear and the potential intensity, affect the transition probability from seeds to TCs. The transition probability is important to consider when explaining the annual cycle (Yang et al. 2021), the interannual variability (Ikehata and Satoh 2021), and the response to strongly patterned SST perturbation (Hsieh et al. 2022) of TC frequency. In this study, we perform experiments with uniform SST increase and focus on the response of TC seeds to radiative heating rate anomalies.

The spatial and temporal frequency of TC seeds can be parameterized by the large-scale circulation using the seed propensity index (SPI) defined in Hsieh et al. (2022). The SPI is an analytical function of large-scale vertical velocity and absolute vorticity derived from the vorticity equation (Hsieh et al. 2020). In the convectively active regions, such as the western Pacific warm pool and the intertropical convergence zone (ITCZ), large-scale vertical velocity approximates the convective mass flux (Held and Zhao 2011), and it obeys the large-scale energy balance expressed in the gross moist stability (GMS) framework (Hsieh et al. 2020). In the GMS framework, vertical velocity balances with net moist static energy flux convergence into the atmospheric column divided by GMS (Neelin and Held 1987). Diagnoses of the large-scale moist static energy budget show that radiative fluxes are important contributors to the net energy flux in active TC seasons (Hsieh et al. 2020). Therefore, the argument predicts, and we seek to test, that *in active TC regions and seasons, anomalous radiative heating tends to increase local TC seed frequency, and anomalous radiative cooling tends to decrease local TC seed frequency*.

To test our hypothesis, we perform model experiments in which the radiative heating rate in the atmosphere is prescribed. In full complexity global climate models and in the real world, the radiative heating rate depends on the temperature and concentration of clouds, aerosols, and greenhouse gases. Our experiment design removes the dependence of radiation on these elements, allowing one to examine the impact of a specific radiation pattern on TC frequency.

This radiation override technique has been used to study the interaction of clouds and water vapor with radiation in mechanism-denial experiments (Wing et al. 2016; Zhang et al. 2021a,b; Wu et al. 2021). In this study, we use this technique for a different purpose—to control for the large-scale pattern of net atmospheric radiative heating rates. It has a side effect of removing the interaction of clouds and water vapor with radiation. As shown in Zhang et al. (2021b), this technique reduces the global TC number by about 20%. Nevertheless, the majority of TCs are able to form because the surface flux feedback is still present. The geographic distribution of TCs with prescribed climatological radiation is similar to that in the default experiment with interactive radiation (Zhang et al. 2021b).

The prescribed radiative heating rates are derived from the HiRAM and AM2.5 atmospheric models with interactive radiation. By interchanging the anomalous radiative heating rates in response to uniform SST increase, we test whether the model spread in TC frequency may be reduced.

2. Theory

In a recently developed framework, the percentage change in TC frequency is approximated as the sum of the percentage change in seed frequency and the percentage change in transition probability (Vecchi et al. 2019; Hsieh et al. 2020; Yang et al. 2021; Hsieh et al. 2022):

$$\frac{\Delta N_{\mathrm{TC}}}{N_{\mathrm{TC}}} \approx \frac{\Delta N_{\mathrm{seed}}}{N_{\mathrm{seed}}} + \frac{\Delta p}{p}, \tag{1}$$

where N_{TC} and N_{seed} denote the frequency of TCs and seeds, respectively, and p denotes the probability of transition from seeds to TCs. The approximation ignores the product of the two fractions on the right-hand side. In response to uniform warming, the percentage change in p is smaller than that in N_{seed}, so the percentage change in N_{TC} is highly correlated with that in N_{seed} (Hsieh et al. 2022).

Hsieh et al. (2022) showed that the percentage change in seed frequency can be parameterized by the percentage change in the seed propensity index (SPI) across models and climates:

$$\frac{\Delta N_{\mathrm{seed}}}{N_{\mathrm{seed}}} \approx \frac{\Delta S}{S}, \tag{2a}$$

$$\text{where } S \equiv (-\omega)^{\uparrow} \frac{1}{1 + Z^{-1/\alpha}}, \text{ and} \tag{2b}$$

$$\text{where } Z \equiv \frac{f + \zeta}{\sqrt{|\beta + \partial_y \zeta| U}}. \tag{2c}$$

In these equations, S denotes SPI, and ω denotes monthly mean vertical velocity at 500 hPa in pressure coordinates. The upward arrow indicates that only the ascending vertical velocity is considered, and the descending vertical velocity is set to zero. The Coriolis parameter and its meridional gradient are denoted by f and β, and the monthly mean relative vorticity at 850 hPa is denoted by ζ. Fitting parameters $U = 20\ \mathrm{m\ s^{-1}}$ and $\alpha = 0.69$ are determined in Hsieh et al. (2020) and are constant across models and climates. The nondimensional parameter Z characterizes tropical regimes dominated by vortices (where $Z \gg 1$) or waves (where $Z \ll 1$).

In the gross moist stability framework (Neelin and Held 1987), $(-\omega)$ is associated with the large-scale energy balance via

$$-\omega \approx \frac{F}{M} \approx \frac{F_{\mathrm{lw}} + F_{\mathrm{sw}} + F_{\mathrm{evap}} + F_{\mathrm{sens}}}{M}, \tag{3}$$

where F is the net vertical moist static energy flux convergence into the atmosphere, and F_{lw}, F_{sw}, F_{evap}, and F_{sens} are the longwave and shortwave radiative flux convergence, the

surface latent heat flux (equivalent to the surface evaporation rate multiplied by the latent heat of vaporization), and the surface sensible heat flux, respectively. The approximation neglects the horizontal energy fluxes, but we will show later that the model differences in ω can be explained by the vertical energy fluxes. The gross moist stability is denoted by M and is diagnosed as $(h_{\text{upper}} - h_{\text{lower}})/g$ following Hsieh et al. (2020), where h is moist static energy, averaged, respectively, between upper (350–150 hPa) and lower (900–750 hPa) levels.

In the western North Pacific, the change in SPI with uniform SST increase is dominated by the change in ω:

$$\Delta S \approx \Delta(-\omega)^{\uparrow} \frac{1}{1 + Z^{-1/\alpha}}. \tag{4}$$

Combining Eqs. (3) and (4),

$$\Delta S \approx \Delta(-\omega)^{\uparrow} \frac{1}{1 + Z^{-1/\alpha}} \approx \Delta\left(\frac{F}{M}\right)^{\uparrow} \frac{1}{1 + Z^{-1/\alpha}}, \tag{5a}$$

$$\approx \left(\frac{\Delta F}{M} + F\Delta\frac{1}{M}\right)^{\uparrow} \frac{1}{1 + Z^{-1/\alpha}}, \quad \text{and} \tag{5b}$$

$$= \left(\frac{\Delta F_{\text{lw}}}{M} + \frac{\Delta F_{\text{sw}}}{M} + \frac{\Delta F_{\text{evap}}}{M} + \frac{\Delta F_{\text{sens}}}{M} + F\Delta\frac{1}{M}\right)^{\uparrow} \frac{1}{1 + Z^{-1/\alpha}}. \tag{5c}$$

Variables without a prefixing Δ are evaluated in the control climate. We will show that $\Delta F_{\text{sens}}/M$ and $F\Delta(1/M)$ are relatively unimportant terms in Eq. (5c) in the western North Pacific. In regions having an ITCZ shift, the change in M and ζ (inside the Z parameter) cannot be neglected, and the full Eq. (2) should be used to explain the change in TC seeds, as done in Hsieh et al. (2020). They showed that the full SPI explains the increase in seed frequency with a poleward shift of the ITCZ.

The surface latent heat flux F_{evap} is an important term in Eq. (5c). Its percentage change can be approximated using the bulk aerodynamic formula following Held and Soden (2000):

$$\frac{\Delta F_{\text{evap}}}{F_{\text{evap}}} \approx \frac{\Delta u}{u} + \frac{\Delta q^*}{q^*} + \frac{\Delta(1 - \text{RH})}{1 - \text{RH}}, \tag{6}$$

where u is near-surface wind speed, q^* is saturation specific humidity at surface temperature, and RH is near-surface relative humidity. The approximation ignores products between any two terms or among all three terms on the right-hand side. The q^* term changes with surface temperature following the Clausius–Clapeyron equation, while the changes in wind and relative humidity are less constrained by theory. In our experiments, F_{lw} and F_{sw} are prescribed, while F_{evap} evolves dynamically. Their combined effect determines N_{seed} and in turn, N_{TC}.

3. Methods

a. Models and tracking algorithms

We use two global atmospheric models developed at the Geophysical Fluid Dynamics Laboratory that have been used extensively for TC modeling, including HiRAM (Zhao et al. 2009) and AM2.5 [the atmosphere component of CM2.5 (Delworth et al. 2012) and Forecast-Oriented Low Ocean Resolution model (Vecchi et al. 2014)]. The model setup is identical to that reported in Hsieh et al. (2022) and is briefly summarized here. The two models have the same resolution, approximately 50 km horizontally on the cubed-sphere grid (Putman and Lin 2007). They have the same parameterization schemes for radiation, cloud microphysics, boundary layer turbulence, and surface fluxes. The most important difference between these two models is the parameterization of convection: HiRAM utilizes a shallow cumulus scheme based on Bretherton et al. (2004), and AM2.5 utilizes a relaxed Arakawa–Schubert scheme based on Moorthi and Suarez (1992). When prescribed with the historical SST time series, both models generate realistic annual cycles (Yang et al. 2021) and geographic distributions (Hsieh et al. 2022) of TCs compared with observations.

The tracking algorithms for TCs and seeds are identical to those used in Hsieh et al. (2022) and are briefly summarized here. The TC tracker, developed by Harris et al. (2016), first identifies local minima in 6-hourly snapshots of sea level pressure and then connects them in time based on the direction of background winds and the movement of the storm in previous snapshots. Additional criteria on surface wind speed, 850-hPa vorticity, lifetime, and radial temperature gradient are applied to identify sustained warm-core cyclones using the same thresholds as in Yang et al. (2021).

The seed tracker, documented in Hsieh et al. (2020) and publicly available through Hsieh (2022), tracks convection aggregates in 6-hourly snapshots of precipitation rates. A convection aggregate in this context refers to contiguous grid boxes with precipitation rates greater than the 99.5th percentile and a diameter greater than 100 km. A seed is defined as a convection aggregate whose maximum 850-hPa vorticity is greater than $4 \times 10^{-4}\ \text{s}^{-1}$ at any instance during its lifetime in the 50-km model. Convection aggregates below this vorticity threshold are regarded as pre-seed disturbances.

b. Experiments

Ten experiments are performed, including four with interactive radiation and six with prescribed radiation, as summarized in Table 1. To increase the statistical significance of TC and seed signals, the annual cycles of the prescribed SST and radiation fields are repeated 50 times, and the last 40 years are analyzed.

The control SST is derived from observations averaged between 1986 and 2005. The +2 K experiments are forced with the control SST plus 2 K everywhere over the ocean. Identical SST fields are applied to both models. More detail on the construction of the prescribed SST is given in Vecchi et al. (2019).

The four-dimensional (x, y, z, t) radiative heating rates are diagnosed from the four interactive radiation experiments, denoted by F^H_{CTL}, F^A_{CTL}, $F^H_{+2\text{K}}$, and $F^A_{+2\text{K}}$ in Table 1. The superscript indicates the model, and the subscript indicates the SST. Their monthly mean is averaged over the last 20 years, before being linearly interpolated to the model

TABLE 1. Radiative heating rates in the interactive radiation experiments (F^H_{CTL}, F^A_{CTL}, $F^H_{+2\mathrm{K}}$, and $F^A_{+2\mathrm{K}}$) and their climatological mean annual cycles ($\overline{F}^H_{\mathrm{CTL}}$, $\overline{F}^A_{\mathrm{CTL}}$, $\overline{F}^H_{+2\mathrm{K}}$, and $\overline{F}^A_{+2\mathrm{K}}$). In the interactive radiation experiments, the radiative heating rates are diagnosed; in the radiation override experiments, the radiative heating rates are prescribed.

SST	Model: HiRAM	Model: AM2.5
	Interactive radiation experiments	
Control	F^H_{CTL}	F^A_{CTL}
+2 K	$F^H_{+2\mathrm{K}}$	$F^A_{+2\mathrm{K}}$
	Radiation self-override experiments	
Control	$\overline{F}^H_{\mathrm{CTL}}$	$\overline{F}^A_{\mathrm{CTL}}$
+2 K	$\overline{F}^H_{+2\mathrm{K}}$	$\overline{F}^A_{+2\mathrm{K}}$
	Radiation cross-override experiments	
+2 K	$\overline{F}^H_{\mathrm{CTL}} + (\overline{F}^A_{+2\mathrm{K}} - \overline{F}^A_{\mathrm{CTL}})$	$\overline{F}^A_{\mathrm{CTL}} + (\overline{F}^H_{+2\mathrm{K}} - \overline{F}^H_{\mathrm{CTL}})$

time step assuming repeated annual cycles, denoted by $\overline{F}^H_{\mathrm{CTL}}$, $\overline{F}^A_{\mathrm{CTL}}$, $\overline{F}^H_{+2\mathrm{K}}$, and $\overline{F}^A_{+2\mathrm{K}}$.

In the "radiation self-override experiments," $\overline{F}^H_{\mathrm{CTL}}$ and $\overline{F}^A_{\mathrm{CTL}}$ are prescribed, respectively, to HiRAM and AM2.5 with the control SST. Similarly, $\overline{F}^H_{+2\mathrm{K}}$ and $\overline{F}^A_{+2\mathrm{K}}$ are prescribed, respectively, to HiRAM and AM2.5 with the +2 K SST. This procedure removes small-scale perturbations in radiative heating rates due to changes in clouds and greenhouse gases while preserving the large-scale patterns and annual cycles, following Zhang et al. (2021a,b).

In the "radiation cross-override experiments," a model is prescribed with the radiative heating rate *anomalies* from the other model. The radiative heating rate anomalies are defined as the difference between the +2 K and control SST simulations using the same model. For HiRAM, the AM2.5 radiative heating rate anomalies ($\overline{F}^A_{+2\mathrm{K}} - \overline{F}^A_{\mathrm{CTL}}$) are added to HiRAM's control radiative heating rate climatology ($\overline{F}^H_{\mathrm{CTL}}$). This procedure ensures that the increased radiative cooling with +2 K is balanced with the increased surface fluxes with +2 K, creating a climatically plausible large-scale environment in which TCs and seeds evolve. A similar procedure is applied to AM2.5, which is prescribed with the radiative heating rate ($\overline{F}^A_{\mathrm{CTL}} + \overline{F}^H_{+2\mathrm{K}} - \overline{F}^H_{\mathrm{CTL}}$).

4. Results

a. Radiative heating rate anomalies, TC seeds, and TCs

In this section, we compare the radiative heating rate anomalies, TC seed frequency, and TC frequency in response to uniform +2 K in SST given by the two models. We then analyze the influence of the prescribed anomalies on seed frequency using the theory outlined in section 2.

Figure 1 shows the anomalous radiative heating rate given by the two models with interactive radiation. The radiative heating rate is integrated over the atmospheric column and weighted by mass and is averaged over the active TC season (July–October). The anomalies are negative (blue) in most regions, indicating anomalous radiative cooling due to SST increase. Even though the global-mean radiative heating rate anomalies are similar (−3.1 W m^{-2} for HiRAM and −3.2 W m^{-2} for AM2.5), the spatial patterns are different due to the different bulk detrainment rates associated with the convection schemes (Zhao et al. 2016). The two models show the largest difference over the western North Pacific region outlined in Fig. 1, where HiRAM shows anomalous cooling and AM2.5 shows anomalous heating.

Figure 2 summarizes the response of seed and TC frequency over all months for the interactive radiation, radiation self-override, and radiation cross-override experiments. The response to +2 K is evaluated with respect to the control SST experiment with the same radiation setup. The bars represent the seed response, and the circles represent the TC response. The seed response has a strong influence on the TC response

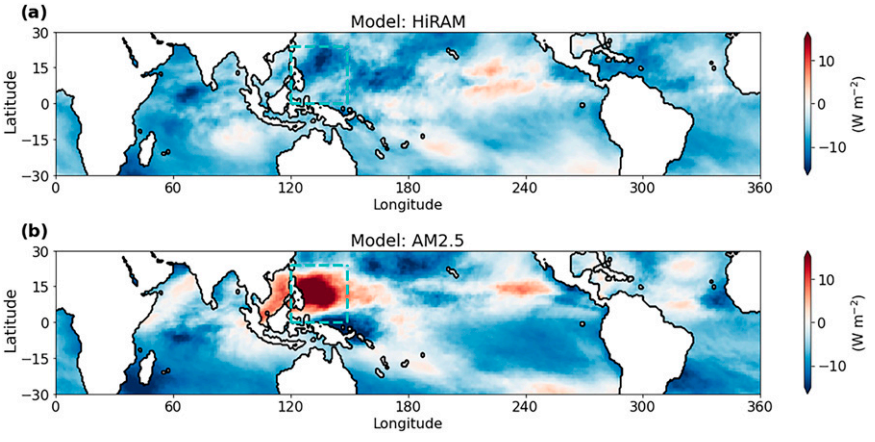

FIG. 1. Vertically integrated radiative heating rate anomalies between +2 K and control SST in the peak Northern Hemispheric tropical cyclone season (July–October). The boxed area in the western North Pacific (0°–25°N, 120°–150°E) highlights the model difference and is the focus of analysis in this study.

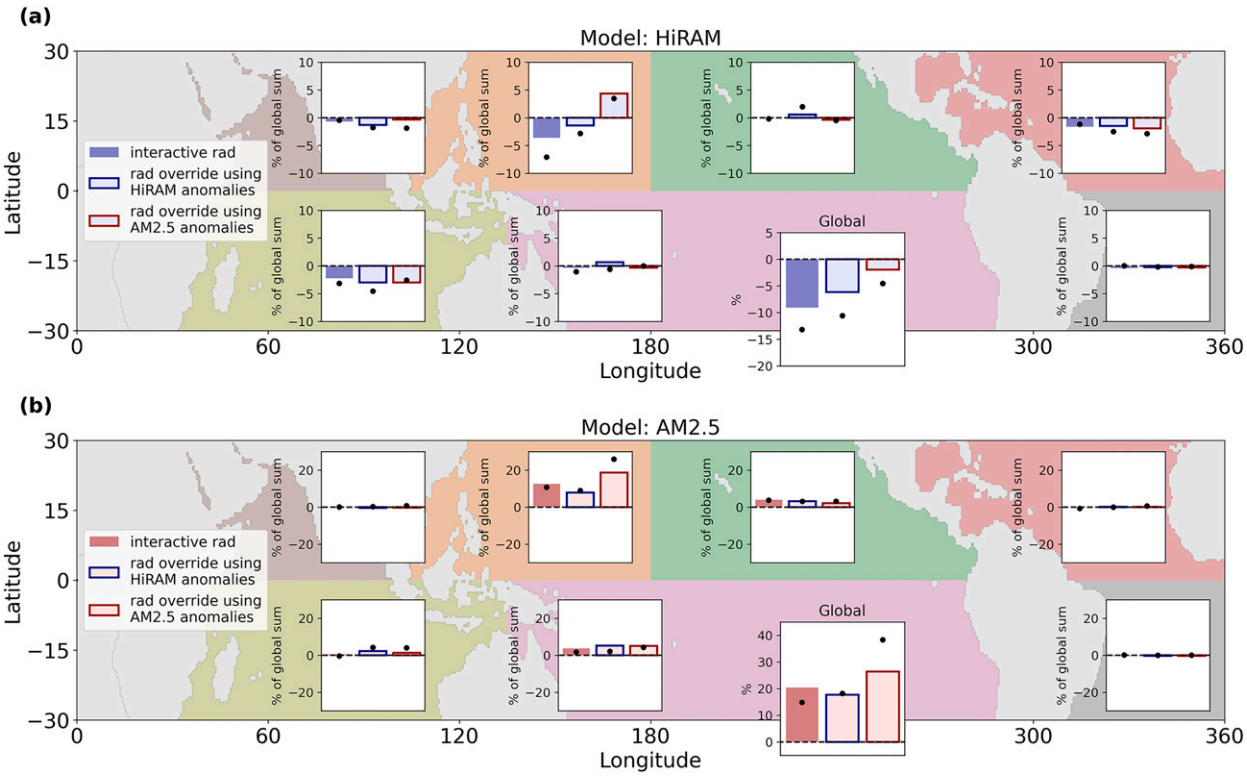

FIG. 2. The response of seed (bars) and tropical cyclone (circles) frequency in the interactive radiation and radiation override experiments. Contribution of each basin to the global percentage change from control to +2 K SST is shown. The bar color indicates the model, and the border color indicates the prescribed radiative heating rate anomalies.

in every basin regardless of using interactive or prescribed radiation.

Comparing the two models with interactive radiation (bars without borders in Figs. 2a,b), they are the most different in the western North Pacific, similar to the difference in the radiation anomalies (Fig. 1). In this region, HiRAM shows decreasing seed frequency and AM2.5 shows increasing seed frequency with warming.

For the radiation override experiments (bars with borders), the response of seeds to SST is altered by the prescribed radiative heating rates. For HiRAM, when the radiation anomalies from its own interactive radiation experiments are prescribed (i.e., self-override), the seed frequency decreases with +2 K in the western North Pacific (blue bars with blue borders in Fig. 2a). But when the radiation anomalies from AM2.5 are prescribed to HiRAM (i.e., cross override), the seed frequency increases with +2 K in this basin (blue bars with red borders in Fig. 2a). The difference between the self-override and the cross-override experiments is less distinct in other ocean basins because the radiative heating rate anomalies there are similar. The results show that it is possible to flip the sign of the seed frequency response through large-scale radiative heating rate anomalies.

Similar results occur in AM2.5. When prescribed with the AM2.5 radiation anomalies (self-override, red bars with red borders in Fig. 2b), the seed frequency increases significantly with +2 K in the western North Pacific, while it increases less when prescribed with the HiRAM radiation anomalies (cross override, red bars with blue borders in Fig. 2b). In summary, prescribing AM2.5 radiation anomalies (net heating) leads to a larger increase in seed frequency in the western North Pacific than prescribing HiRAM radiation anomalies (net cooling) for both models.

b. *The SPI and GMS diagnostics*

To explain how large-scale radiative heating rates influence TC seed frequency, terms in Eq. (5) are diagnosed and shown in Fig. 3. For clarity, the upward arrow symbol is omitted in the following figures and formulas. These quantities are averaged over the boxed area in the western North Pacific shown in Fig. 1 over July–October to emphasize the model difference. In the interactive radiation experiments, the approximated SPI decreases in HiRAM and increases in AM2.5 (the left most bars in Fig. 3a), consistent with the response of seed frequency in the respective model.

The model difference in $(-\Delta\omega)(1 + Z^{-1/\alpha})^{-1}$ is generally captured by the model difference in $\Delta(F/M)(1 + Z^{-1/\alpha})^{-1}$. There is some mismatch due to the omission of horizontal fluxes and the limited vertical levels from which M is calculated. Nevertheless, the vertical fluxes diagnosed here have shown a leading-order impact on ω and SPI.

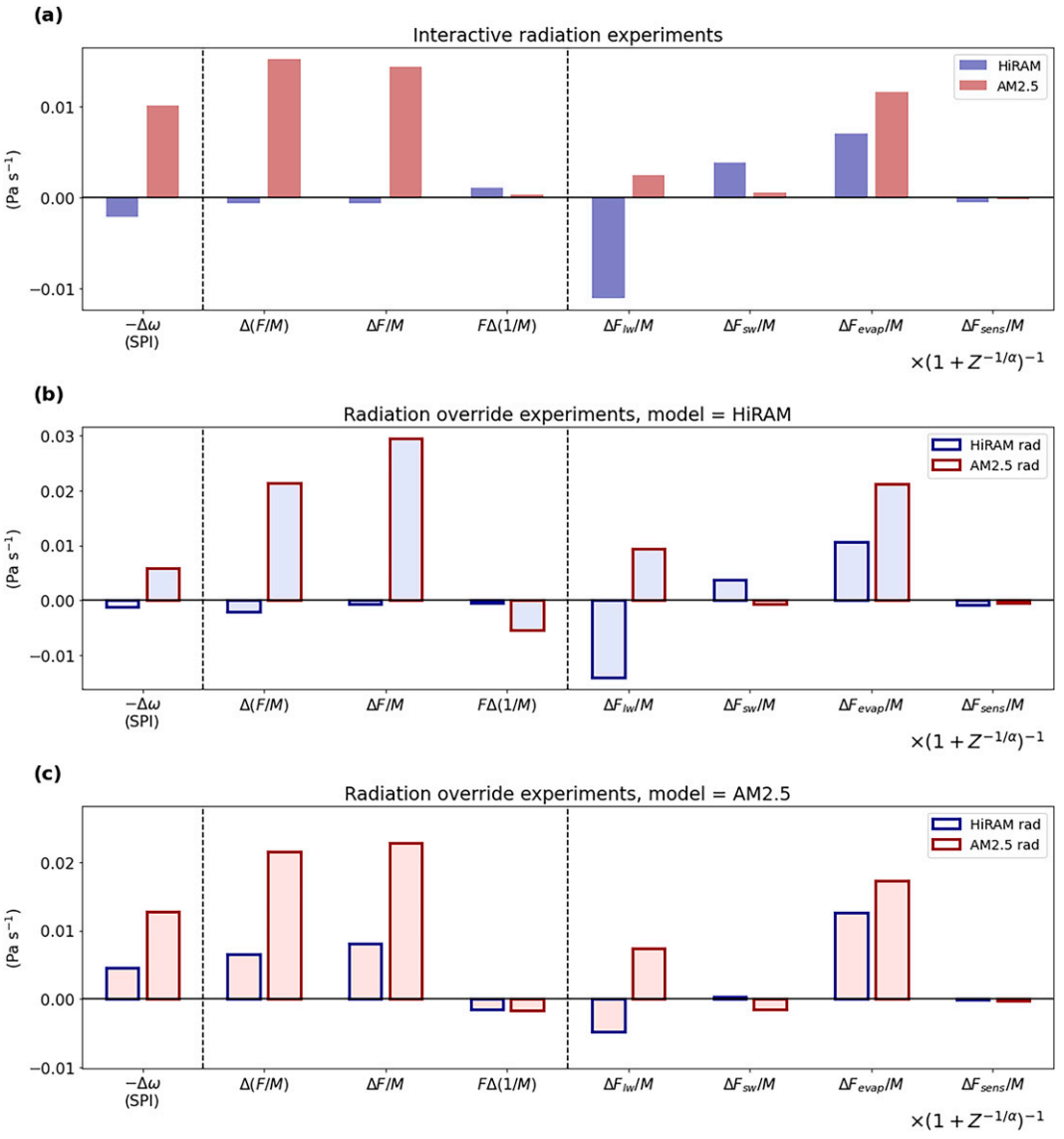

FIG. 3. The SPI decomposed using Eq. (5), for (a) interactive radiation experiments, and radiation override experiments using (b) the HiRAM model and (c) the AM2.5 model. The bar color indicates the model, and the border color indicates the prescribed radiative heating rate anomalies. The differences are taken between the +2 K and control experiments averaged over the western North Pacific box shown in Fig. 1 from July to October. The factor $(1 + Z^{-1/\alpha})^{-1}$ has been multiplied with every term shown, so the left most bars represent the approximated SPI response. The vertical dashed lines separate different groups of decomposition in Eq. (5).

Breaking down $\Delta(F/M)$ by the chain rule and neglecting the higher-order product term, Fig. 3 shows that the change in vertical flux convergence, $\Delta F/M$, is generally larger than the change in gross moist stability, $F\Delta(1/M)$. The fact that $\Delta F/M > F\Delta(1/M)$ is apparent in the spatial map (not shown). In some cases, positive and negative values would cancel when taking the spatial mean, and both $\Delta F/M$ and $F\Delta(1/M)$ would be close to zero (HiRAM in Fig. 3a). That said, the model difference in $\Delta(F/M)$ is well captured by the model difference in $\Delta F/M$ in all experiments.

A further breakdown of ΔF shows that the longwave radiative flux convergence and the surface latent heat flux are the most important changes in the net energy flux convergence. The opposite radiative flux convergence between the models can also be seen in the maps shown in Fig. 1. The surface latent heat flux increases with +2 K in both models but with different magnitudes, which will be further analyzed in the following subsection.

Figure 3b shows the same diagnostics for the radiation override experiments using HiRAM. The shading of the bars represents the underlying model (which is the same for all bars in Fig. 3b), and the color of the bar borders represents the prescribed radiation anomalies. The opposite seed response

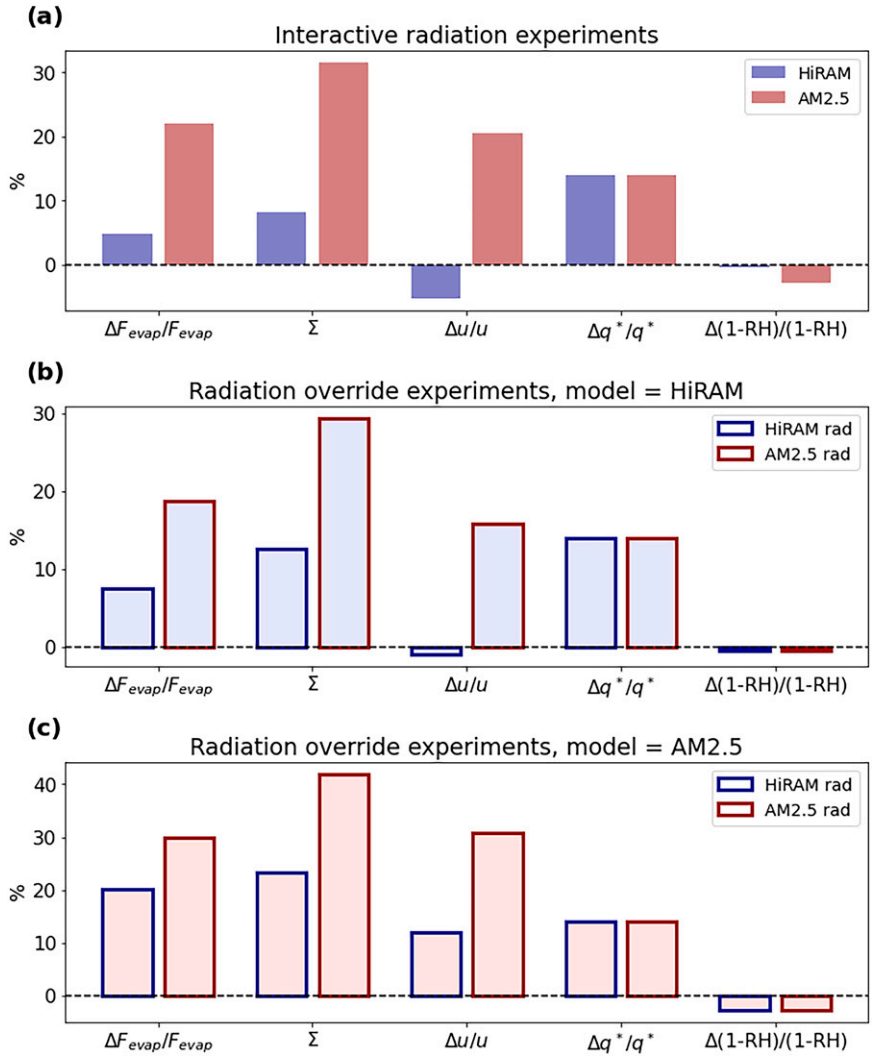

FIG. 4. Breakdown of the percentage change in evaporation for (a) interactive radiation experiments, and radiation override experiments using (b) the HiRAM model and (c) the AM2.5 model. The bar color indicates the model, and the border color indicates the radiation anomaly prescribed. The quantities are averaged over the western North Pacific box shown in Fig. 1 from July to October. The Σ symbol represents the sum of $\Delta u/u$, $\Delta q^*/q^*$, and $\Delta(1 - \mathrm{RH})/(1 - \mathrm{RH})$, namely, the right-hand side of Eq. (6), which approximates $\Delta F_{\mathrm{evap}}/F_{\mathrm{evap}}$ with the omission of cross terms.

to the different radiative heating rate anomalies is captured by the SPI, as well as the GMS approximation indicated by $\Delta(F/M)(1 + Z^{-1/\alpha})^{-1}$.

Figure 3c shows the same diagnostics for AM2.5. Note that ΔF_{lw} and ΔF_{sw} are identical in all three panels by construction, but M can differ slightly depending on the climate. Even though the prescribed radiative heating rate anomalies have opposite signs, they do not lead to opposite SPI changes because of the strong increase in the surface latent heat flux. The sum of all fluxes leads to an increased SPI for both radiation override experiments using AM2.5.

In summary, prescribing AM2.5 radiation anomalies leads to a larger increase in SPI than prescribing HiRAM radiation anomalies, consistent with the seed frequency response.

c. *Breakdown of the surface latent heat flux response*

The surface latent heat flux, or the surface evaporation rate multiplied by the latent heat of vaporization, is an important term in the moist static energy budget. The factors influencing the evaporation rate in Eq. (6) are analyzed in Fig. 4. Similar to the previous subsection, the variables are averaged over the western North Pacific box shown in Fig. 1 from July to October to highlight the model difference. The color coding follows that in previous figures: the shading represents the underlying model, and the border represents the prescribed radiation anomalies.

Figure 4a shows the percentage change in evaporation rates in the interactive radiation experiments. It also shows contributions from the percentage changes in surface wind speed, saturation

specific humidity, and one minus relative humidity. The sum of the contribution terms captures the stronger evaporation rate increase in AM2.5 than that in HiRAM. There is less than a 10% error from the omitted product terms, and the majority of the model difference is captured by the terms shown. The increase in evaporation rate in AM2.5 is approximately 4 times the increase in HiRAM.

Among the three contribution terms, surface wind speed and saturation specific humidity change more significantly than relative humidity does. The change in saturation specific humidity is estimated by the Clausius–Clapeyron scaling with +2 K and is the same in both models. The change in surface wind speed has opposite signs between models. The signs are consistent with the change in seed frequency: a decrease in HiRAM and an increase in AM2.5. This consistency may be interpreted as the surface flux feedback associated with TCs and to some degree with seeds (Zhang et al. 2021b). An increase in seed frequency in AM2.5 corresponds to an increase in the mean surface wind speed, and vice versa for HiRAM.

Figures 4b and 4c show the breakdown of evaporation rates for the radiation override experiments, corresponding to the experiments in Figs. 3b and 3c. A similar reasoning applies to these results. The change in the evaporation rate is dominated by the changes in saturation specific humidity and surface wind speed. The change in surface wind speed is consistent with the change in seed frequency. The evaporation rate in the experiment prescribed with the AM2.5 radiative heating rate anomalies increases more than that prescribed with the HiRAM anomalies.

The analysis explains why the prescribed radiation is able to flip the sign of the western North Pacific seed response in HiRAM but not in AM2.5. The Clausius–Clapeyron scaling tends to increase the surface evaporation rate with warming. For HiRAM prescribed with the AM2.5 radiation anomalies, both ΔF_{lw} and ΔF_{evap} increase, flipping the sign and leading to an increase in SPI (blue bars with red borders in Fig. 3b). For AM2.5 prescribed with the HiRAM radiation anomalies, the decrease in ΔF_{lw} is less significant than the increase in ΔF_{evap}, adding up to a smaller increase in SPI (red bars with blue borders in Fig. 3c) than its radiation self-override experiment.

As a side note, the breakdown of evaporation rates in the global mean is different from that in the western North Pacific region. The percentage changes in saturation specific humidity and near-surface relative humidity are more significant in the global mean, while the percentage change in near-surface wind speed is small. The near-surface relative humidity increases in both models, leading to a decrease in $\Delta(1 - \mathrm{RH})/(1 - \mathrm{RH})$, while the saturation specific humidity increases follow the Clausius–Clapeyron scaling. The global-mean evaporation rate increases by 6.6% per 2 K in both models, constrained by the global energy balance (Jeevanjee and Romps 2018).

5. Discussion

a. *Large-scale vertical velocity in TC genesis potential indices*

Large-scale vertical velocity is a centerpiece in linking the seed propensity index with the gross moist stability theory. This variable is not commonly used in empirical TC genesis potential indices, as vertical velocity is difficult to observe. Large-scale vertical velocity is better defined in model simulations averaged over a long period of time. This variable has been found to be a strong indicator of the change in TC frequency in the twentieth century reanalysis (Chand et al. 2022) and in global warming simulations (Held and Zhao 2011; Sugi et al. 2012).

In an empirical TC genesis potential index developed using reanalysis products and models (Wang and Murakami 2020), large-scale vertical velocity is found to be a dominant term in explaining simulated future TC frequency (Murakami and Wang 2022). In empirical indices that do not include large-scale vertical velocity as a predictor, the potential intensity may be playing a similar role, as both large-scale vertical velocity and potential intensity depend on air–sea thermodynamic disequilibrium (Emanuel 2022).

b. *Definition of TC seeds*

Our analysis focuses on the frequency of TC seeds, which are emergent structures detected in models. Seeds in our definition are dependent on the large-scale climate, and the frequency can be parameterized by the seed propensity index.

The nomenclature "seed" is used in some studies to refer to the initial condition for a high-resolution, axisymmetric TC intensity model used to downscale TC activity from global models (Emanuel et al. 2008; Emanuel 2013, 2021). The two aforementioned definitions of seeds are not equivalent: the surface wind speeds of the weakest seeds detected in our models are 2 times as large as that of the initial vortex in the axisymmetric TC model.

What the two definitions have in common is the sensitivity of annual cycles to the wind speed threshold for those pre-TC vortices. Emanuel (2022) analyzed annual cycles of pre-TC vortices generated by the axisymmetric TC model. For each wind speed threshold, the frequency of pre-TC vortices stronger than the threshold is calculated. Emanuel (2022) found that the annual cycle becomes sharper as the threshold increases. This sharpening is consistent with the findings of Yang et al. (2021), who detect seeds and TCs using the same method as the present study and found that the annual cycle of TC frequency is sharper than the annual cycle of seed frequency.

c. *Implications for coupled climate models*

The shortwave radiative fluxes are less significant than the longwave radiative fluxes in the atmospheric column energy budget, but they are important in the top-of-atmosphere energy balance. Since the ocean dynamically evolves in a coupled model, the SST will be influenced by the shortwave cloud radiative effect and the surface heat fluxes. When seed frequency increases, the increased shortwave reflection and the increased surface heat fluxes may decrease local SST. This feedback is not captured in an atmospheric model with prescribed SST but would be present in a coupled model.

6. Conclusions

We investigate the influence of large-scale radiative heating rate anomalies on TC frequency by conducting radiation override experiments. Given two models with opposite TC frequency responses to uniform SST warming, we interchange their radiative heating rate anomalies. By design, the prescribed radiation modifies only the mean, balanced vertical velocity, but not the instantaneous, fast-evolving updraft. The results show that TC frequency can be modified by large-scale radiative heating rate anomalies, and that the TC frequency response approximately follows the seed frequency response.

We explain the seed frequency response using a previously developed "seed propensity index" (SPI) that relates seed frequency to large-scale vertical velocity and absolute vorticity. This study further expands large-scale vertical velocity using the gross moist stability theory to express the relationship between seed frequency and large-scale radiative heating rate anomalies. Our theory predicted the sign of seed frequency response to the prescribed radiative heating rate anomalies.

In the western North Pacific region where the models we use are the most inconsistent, the decrease in seed frequency in HiRAM becomes an increase when prescribed with radiative heating rate anomalies from AM2.5 (which is net heating). Similarly, the increase in seed frequency in AM2.5 is reduced when prescribed with radiative heating rate anomalies from HiRAM (which is net cooling). The model spread in SPI and seed frequency response is reduced by the radiation cross-override technique.

Using the radiation override technique, we elucidate the direction of causality, represented by the one-way arrow in Fig. 5. Causality would otherwise be difficult to infer from budget analysis when feedback processes are present, represented by the two-way arrow in Fig. 5. Note that the arrow associated with radiation is one way in the radiation override experiments, but it may be both ways when radiative feedback is permitted. We demonstrate that large-scale vertical velocity can influence seed frequency, but the feedback processes also contribute to the correlation between SPI and seed frequency.

This mechanism can be interpreted as a downscale control, by which climatological fields influence seed and TC genesis on the storm scale. Two large-scale fields are perturbed in our experiments, including the radiative heating rate and SST. The large-scale contribution to moist static energy flux convergence in Eq. (5c) due to the prescribed radiation and the Clausius–Clapeyron scaling can be approximated by $\Delta F_{\mathrm{LS}} = \Delta F_{\mathrm{lw}} + \Delta F_{\mathrm{sw}} + c(\Delta T)F_{\mathrm{evap}}$, where $c = 7\%\ \mathrm{K}^{-1}$. The total ΔF_{LS} is negative in the radiation self-override experiment with HiRAM, contributing to a decrease in SPI in the western North Pacific region. On the other hand, ΔF_{LS} is positive in the radiation cross-override experiment with HiRAM and in both override experiments with AM2.5, contributing to an increase in SPI in the same region in these experiments.

The sign of surface wind speed response is consistent with the sign of seed frequency response across all experiments, suggesting a surface flux feedback associated with the surface winds of seeds and TCs. This is consistent with Wing et al. (2019) and Zhang et al. (2021b), who showed a positive feedback in which surface fluxes amplify the moist static energy variance associated with seeds and TCs.

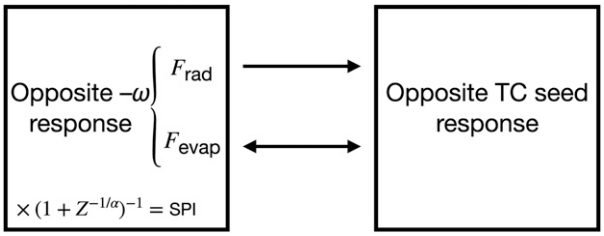

FIG. 5. Causality and feedback in the radiation override experiments. The gross moist stability associates $(-\omega)$ with F_{rad} and F_{evap}, where $F_{\mathrm{rad}} = F_{\mathrm{lw}} + F_{\mathrm{sw}}$. The SPI associates $(-\omega)$ with TC seed frequency. All variables are defined in section 2.

In the broader context, the uncertainty in radiative heating rate anomalies is associated with the uncertainty in the cloud response, which is a major source of uncertainty in climate sensitivity (e.g., Zelinka et al. 2020). It is worth noting that uncertainty in global TC frequency projection dates back at least to the first study of TC response to warming based on global climate models of which we are aware (Broccoli and Manabe 1990), and in that study the TC response depended crucially on the radiative response of the model through either prescribed or interactive clouds. Together with the findings in this study, the implication is that global TC frequency projection and climate sensitivity may be dependent, as they are both related to the cloud response. The relationship will be investigated in a future study.

Acknowledgments. We thank Daniel Chavas and Jie Chen for valuable feedback on earlier versions of the manuscript. This work has been supported by NOAA/MAPP Award NA20OAR4310393, Department of Energy Award DE-SC0021333, and the Carbon Mitigation Initiative at Princeton University. The simulations were performed on computational resources managed and supported by Princeton Research Computing, a consortium of groups including the Princeton Institute for Computational Science and Engineering, the Office of Information Technology's High Performance Computing Center, and the Visualization Laboratory at Princeton University. This publication was supported by the Princeton University Library Open Access Fund.

Data availability statement. Source code of the HiRAM model is available from https://www.gfdl.noaa.gov/hiram-quickstart. Source code of the AM2.5 model is available from https://www.gfdl.noaa.gov/cm2-5-and-flor-quickstart. Python scripts for tracking tropical cyclone seeds and computing the seed propensity index are available from https://github.com/tlhsieh/tropical_cyclone_seeds.

REFERENCES

Bretherton, C. S., J. R. McCaa, and H. Grenier, 2004: A new parameterization for shallow cumulus convection and its application to marine subtropical cloud-topped boundary layers. Part I: Description and 1D results. *Mon. Wea. Rev.*, **132**, 864–882,

https://doi.org/10.1175/1520-0493(2004)132<0864:ANPFSC>2.0.CO;2.

Broccoli, A. J., and S. Manabe, 1990: Can existing climate models be used to study anthropogenic changes in tropical cyclone climate? *Geophys. Res. Lett.*, **17**, 1917–1920, https://doi.org/10.1029/GL017i011p01917.

Chand, S. S., and Coauthors, 2022: Declining tropical cyclone frequency under global warming. *Nat. Climate Change*, **12**, 655–661, https://doi.org/10.1038/s41558-022-01388-4.

Delworth, T. L., and Coauthors, 2012: Simulated climate and climate change in the GFDL CM2.5 high-resolution coupled climate model. *J. Climate*, **25**, 2755–2781, https://doi.org/10.1175/JCLI-D-11-00316.1.

Emanuel, K. A., 2010: Tropical cyclone activity downscaled from NOAA-CIRES reanalysis, 1908–1958. *J. Adv. Model. Earth Syst.*, **2**, 1, https://doi.org/10.3894/JAMES.2010.2.1.

——, 2013: Downscaling CMIP5 climate models shows increased tropical cyclone activity over the 21st century. *Proc. Natl. Acad. Sci. USA*, **110**, 12 219–12 224, https://doi.org/10.1073/pnas.1301293110.

——, 2021: Response of global tropical cyclone activity to increasing CO_2: Results from downscaling CMIP6 models. *J. Climate*, **34**, 57–70, https://doi.org/10.1175/JCLI-D-20-0367.1.

——, 2022: Tropical cyclone seeds, transition probabilities, and genesis. *J. Climate*, **35**, 3557–3566, https://doi.org/10.1175/JCLI-D-21-0922.1.

——, R. Sundararajan, and J. Williams, 2008: Hurricanes and global warming: Results from downscaling IPCC AR4 simulations. *Bull. Amer. Meteor. Soc.*, **89**, 347–368, https://doi.org/10.1175/BAMS-89-3-347.

Harris, L. M., S.-J. Lin, and C. Tu, 2016: High-resolution climate simulations using GFDL HiRAM with a stretched global grid. *J. Climate*, **29**, 4293–4314, https://doi.org/10.1175/JCLI-D-15-0389.1.

Held, I. M., and B. J. Soden, 2000: Water vapor feedback and global warming. *Annu. Rev. Energy Environ.*, **25**, 441–475, https://doi.org/10.1146/annurev.energy.25.1.441.

——, and M. Zhao, 2011: The response of tropical cyclone statistics to an increase in CO_2 with fixed sea surface temperatures. *J. Climate*, **24**, 5353–5364, https://doi.org/10.1175/JCLI-D-11-00050.1.

Hsieh, T.-L., 2022: TLHSIEH/Tropical_cyclone_seeds: Stable release. Zenodo, accessed February 2022, https://doi.org/10.5281/zenodo.6193045.

——, G. A. Vecchi, W. Yang, I. M. Held, and S. T. Garner, 2020: Large-scale control on the frequency of tropical cyclones and seeds: A consistent relationship across a hierarchy of global atmospheric models. *Climate Dyn.*, **55**, 3177–3196, https://doi.org/10.1007/s00382-020-05446-5.

——, W. Yang, G. A. Vecchi, and M. Zhao, 2022: Model spread in the tropical cyclone frequency and seed propensity index across global warming and ENSO-like perturbations. *Geophys. Res. Lett.*, **49**, e2021GL097157, https://doi.org/10.1029/2021GL097157.

Ikehata, K., and M. Satoh, 2021: Climatology of tropical cyclone seed frequency and survival rate in tropical cyclones. *Geophys. Res. Lett.*, **48**, e2021GL093626, https://doi.org/10.1029/2021GL093626.

Jeevanjee, N., and D. M. Romps, 2018: Mean precipitation change from a deepening troposphere. *Proc. Natl. Acad. Sci. USA*, **115**, 11 465–11 470, https://doi.org/10.1073/pnas.1720683115.

Knutson, T., and Coauthors, 2020: Tropical cyclones and climate change assessment: Part II: Projected response to anthropogenic warming. *Bull. Amer. Meteor. Soc.*, **101**, E303–E322, https://doi.org/10.1175/BAMS-D-18-0194.1.

Moorthi, S., and M. J. Suarez, 1992: Relaxed Arakawa-Schubert. A parameterization of moist convection for general circulation models. *Mon. Wea. Rev.*, **120**, 978–1002, https://doi.org/10.1175/1520-0493(1992)120<0978:RASAPO>2.0.CO;2.

Murakami, H., and B. Wang, 2022: Patterns and frequency of projected future tropical cyclone genesis are governed by dynamic effects. *Commun. Earth Environ.*, **3**, 77, https://doi.org/10.1038/s43247-022-00410-z.

Neelin, J. D., and I. M. Held, 1987: Modeling tropical convergence based on the moist static energy budget. *Mon. Wea. Rev.*, **115**, 3–12, https://doi.org/10.1175/1520-0493(1987)115<0003:MTCBOT>2.0.CO;2.

Putman, W. M., and S.-J. Lin, 2007: Finite-volume transport on various cubed-sphere grids. *J. Comput. Phys.*, **227**, 55–78, https://doi.org/10.1016/j.jcp.2007.07.022.

Stevens, B., S. C. Sherwood, S. Bony, and M. J. Webb, 2016: Prospects for narrowing bounds on Earth's equilibrium climate sensitivity. *Earth's Future*, **4**, 512–522, https://doi.org/10.1002/2016EF000376.

Sugi, M., H. Murakami, and J. Yoshimura, 2012: On the mechanism of tropical cyclone frequency changes due to global warming. *J. Meteor. Soc. Japan*, **90A**, 397–408, https://doi.org/10.2151/jmsj.2012-A24.

Vecchi, G. A., and Coauthors, 2014: On the seasonal forecasting of regional tropical cyclone activity. *J. Climate*, **27**, 7994–8016, https://doi.org/10.1175/JCLI-D-14-00158.1.

——, and Coauthors, 2019: Tropical cyclone sensitivities to CO_2 doubling: Roles of atmospheric resolution, synoptic variability and background climate changes. *Climate Dyn.*, **53**, 5999–6033, https://doi.org/10.1007/s00382-019-04913-y.

Wang, B., and H. Murakami, 2020: Dynamic genesis potential index for diagnosing present-day and future global tropical cyclone genesis. *Environ. Res. Lett.*, **15**, 114008, https://doi.org/10.1088/1748-9326/abbb01.

Wing, A. A., S. J. Camargo, and A. H. Sobel, 2016: Role of radiative–convective feedbacks in spontaneous tropical cyclogenesis in idealized numerical simulations. *J. Atmos. Sci.*, **73**, 2633–2642, https://doi.org/10.1175/JAS-D-15-0380.1.

——, and Coauthors, 2019: Moist static energy budget analysis of tropical cyclone intensification in high-resolution climate models. *J. Climate*, **32**, 6071–6095, https://doi.org/10.1175/JCLI-D-18-0599.1.

Wu, S.-N., B. J. Soden, and D. S. Nolan, 2021: Examining the role of cloud radiative interactions in tropical cyclone development using satellite measurements and WRF simulations. *Geophys. Res. Lett.*, **48**, e2021GL093259, https://doi.org/10.1029/2021GL093259.

Yamada, Y., and Coauthors, 2021: Evaluation of the contribution of tropical cyclone seeds to changes in tropical cyclone frequency due to global warming in high-resolution multi-model ensemble simulations. *Prog. Earth Planet. Sci.*, **8**, 11, https://doi.org/10.1186/s40645-020-00397-1.

Yang, W., T.-L. Hsieh, and G. A. Vecchi, 2021: Hurricane annual cycle controlled by both seeds and genesis probability. *Proc. Natl. Acad. Sci. USA*, **118**, e2108397118, https://doi.org/10.1073/pnas.2108397118.

Zelinka, M. D., T. A. Myers, D. T. McCoy, S. Po-Chedley, P. M. Caldwell, P. Ceppi, S. A. Klein, and K. E. Taylor, 2020: Causes of higher climate sensitivity in CMIP6 models. *Geophys. Res. Lett.*, **47**, e2019GL085782, https://doi.org/10.1029/2019GL085782.

Zhang, B., B. J. Soden, G. A. Vecchi, and W. Yang, 2021a: Investigating the causes and impacts of convective aggregation in a high resolution atmospheric GCM. *J. Adv. Model. Earth Syst.*, **13**, e2021MS002675, https://doi.org/10.1029/2021MS002675.

——, ——, ——, and ——, 2021b: The role of radiative interactions in tropical cyclone development under realistic boundary conditions. *J. Climate*, **34**, 2079–2091, https://doi.org/10.1175/JCLI-D-20-0574.1.

Zhao, M., I. M. Held, S.-J. Lin, and G. A. Vecchi, 2009: Simulations of global hurricane climatology, interannual variability, and response to global warming using a 50-km resolution GCM. *J. Climate*, **22**, 6653–6678, https://doi.org/10.1175/2009JCLI3049.1.

——, and Coauthors, 2016: Uncertainty in model climate sensitivity traced to representations of cumulus precipitation microphysics. *J. Climate*, **29**, 543–560, https://doi.org/10.1175/JCLI-D-15-0191.1.